Electrochimica Acta 251 (2017) 638–650

Contents lists available at ScienceDirect

Electrochimica Acta

journal homepage: www.elsevier.com/locate/electacta

Research Paper

MOF derived Mesoporous Nitrogen doped Carbons with high Activity towards Oxygen Reduction

Ana Katherine Díaz-Duran, Federico Roncaroli*

Departamento de Física de la Materia Condensada, Centro Atómico Constituyentes, Comisión Nacional de Energía Atómica (CNEA), Avenida General Paz 1499, 1650, San Martín, Buenos Aires, Argentina
Departamento de Química Inorgánica Analítica y Química Física, Facultad de Ciencias Exactas y Naturales, Universidad de Buenos Aires, Ciudad Universitaria, Pabellón II, 1428, Ciudad de Buenos Aires, Argentina
Consejo Nacional de Investigaciones Científicas y Técnicas-CONICET, Godoy Cruz 2290, 1425, Ciudad de Buenos Aires, Argentina

ARTICLE INFO

Article history:
Received 5 June 2017
Received in revised form 4 August 2017
Accepted 9 August 2017
Available online 14 August 2017

Keywords:
metal organic framework
polymer electrolyte membrane
fuel cell
non-noble catalyst
Platinum-free
coordination polymer

ABSTRACT

In order to obtain Platinum-free catalysts for the Oxygen Reduction Reaction (ORR) in Fuel Cells, Nitrogen doped mesoporous carbons were prepared from pyrolysis of three Cobalt metal organic frameworks (MOFs), one linear coordination polymer and one complex. Electron micrographs revealed the presence of pores of different sizes in the samples. Particles resembled polyhedrons, sponges, bars, etc. The catalyst derived from Cobalt 2,3-pyrazinedicarboxylate polymer (700 °C) exhibited attractive electrokinetic parameters for the ORR comparable to those of Pt 20% in acidic medium (Tafel slope = 82 mV dec^{-1}, exchange current density = 10 mA cm^{-1}, equilibrium potential = 907 mV (vs RHE), half wave potential = 720 mV (vs RHE), number of exchanged electrons *ca.* 4.0, 0.5 M H_2SO_4). Limiting current and H_2O_2 yield (< 10%) are similar to those of ZIF-67 derived materials. The half wave potential is shifted to 820 mv (vs RHE) in alkaline medium (0.1 M KOH). The former sample holds a surface area on mesopores which duplicates that of the ZIF-67 700 °C. A correlation was found between the current intensity for the ORR and the mesopore area occupied by N (%N x specific area on mesopores). The Cobalt 2,3-pyrazinedicarboxylate derived material (700 °C) showed high methanol tolerance compared to Pt 20% (0.05 M methanol, 0.5 M H_2SO_4), and good ORR durability (after 3000 cycles between 0.25–1.15 V vs RHE, O_2 saturated 0.5M H_2SO_4).

1. Introduction

The increasing world demand of energy has supported the search and development of new materials for chemical energy conversion and storage. This parallels the generation of greenhouse effect gases, particularly CO_2, from the combustion of fossil fuels. In this way, fuel cells, particularly H_2/O_2 or H_2/air cells, have emerged as promising candidates to supply energy to vehicles and to convert H_2 (with O_2 or air) into energy produced from intermittent renewable sources such as sunlight, wind, tides and waves [1].

Among the fuel cells that convert the energy of the reaction between H_2 and O_2 into electricity, Proton Exchange or Polymer Electrolyte Membrane fuel cells (PEM FC) operate at a relatively low temperature, ca 100 °C [2]. On both cathodic and anodic electrodes, they usually employ Platinum or noble metal nanoparticles supported on carbon as catalysts. The high cost and low abundance of these metals, that prevents the massive productions or distributions of the PEM cells in the market, have promoted the search of non-noble or Platinum-free catalyst. This is particularly relevant for the cathode catalyst, since the Oxygen Reduction Reaction (ORR) is kinetically slower than the oxidation of H_2 and higher loads of catalyst are necessary. Platinum catalysts have an additional limitation which is their strong sensibility towards CO traces present in H_2 gas (obtained by reforming), and cross over effects (if methanol is used in the anode instead of H_2) [2,3].

Since the discovery in the 60's that Co phthalocyanines catalyze the ORR, and inspired in the active site of cytochrome C oxidase, which holds an Fe-heme active site, much work has been done employing Co and Fe complexes with macrocycles, like porphyrins and other nitrogenated ligands, as catalysts for the ORR. Later, it was found that the pyrolysis products of these compounds, as well as other complexes obtained from Co and Fe salts, N-donor ligands and/or polymers, supported on different carbons displayed a

* Corresponding author.
E-mail address: roncaroli@cnea.gov.ar (F. Roncaroli).

http://dx.doi.org/10.1016/j.electacta.2017.08.055
0013-4686/

higher activity and stability than their precursor materials, comparable in some cases to those of Platinum [3,4].

There is still some controversy about the actual identity of the active sites where the ORR takes place. Many reports support that pyridinic nitrogen atoms, particularly those on metal-free catalysts, are the active sites, which suggest that no metallic atoms are necessary for the ORR to occur [5]. On the other hand, studies conducted on Fe and Co compounds as catalyst precursors, employing Mössbauer and X-ray absorption spectroscopies, support the idea that Fe-N_x or Co-N_x moieties with coordinated pyridinic N atoms correspond to the active sites [6], and are indeed necessary for the reduction of O_2 directly to water in a 4 e^- reaction, or, at least, to reduce H_2O_2 to water [7–10]. In opposition to those findings, a highly active Fe-based catalysts has been reported, where no direct metal-nitrogen coordination was shown using in situ spectroscopic techniques [11].

More recently, Metal Organic Frameworks (MOFs) and Coordination Polymers have been used as sacrificial templates or precursor materials to generate porous carbons with different heteroatom doping and/or decorated with metallic/oxide nanoparticles [12]. According to IUPAC recommendations 2013 [13], a Coordination Polymer is a Coordination Compound (complex) with repeating coordination entities extending in one, two or three dimensions. In a Coordination Network the coordination polymer extends in two or three dimensions. A Metal Organic Framework (MOF) is a coordination network with organic ligands containing potential voids [13]. In general, they are crystalline microporous materials [14]. The possibility to choose the organic ligand or linker and the metal ions, allows tuning the structure, pore size, surface area and multiple functionalities in a rational way [14,15]. In this way, applications of MOFs have been proposed for: gas storage and separation, drug delivery, sensors, catalysis and optoelectronic devices [16]. Porous carbons derived from MOFs have been reported with possible application for: H_2 storage, sensors, supercapacitors and lithium batteries [17–19]. Most of the studies on ORR have been conducted on the Zeolitic Imidazolate Frameworks (ZIFs) with different metals like Co (ZIF-67 and ZIF-9), Zn (ZIF-8) and Fe, where the ligands contribute to the carbonaceous matrix and they are the N source [12]. The metal ions, in turn, generate oxide particles or they are reduced to metallic nanoparticles during thermal treatment or pyrolysis [12,20].

In the present study mesoporous N-doped carbons from three metal organic frameworks (MOFs), one linear coordination polymer and one complex were synthesized as catalyst precursors for the ORR. In order to facilitate the formation of CoN_4 sites and pyridinic N atoms on the particle surface, Co^{2+} was used as metal source and five different N-heterocyclic ligands were employed, particularly pyridine and pyrazine substituted rings. ZIF-67 was also included for comparison. They were submitted to two thermal treatments (700 or 900 °C), and finally leached with acid and dried. The carbonaceous products exhibited different morphologies, and they were studied through microscopies and several physical and electrochemical techniques. A detailed study of the catalytic activity for ORR as a function of the physical parameters, namely: BET surface area, N and Co content and pore structure is presented. The results are relevant for the design of new catalysts. These new mesoporous materials may be useful in other energy convertor or storage devices where fast diffusion to active sites in required.

2. Experimental methods

2.1. Chemicals

All of them were analytical grade and used without further purification. Ligands employed for the catalysts synthesis are depicted in the Supplementary Information: 2-Methylimidazole, Nicotinic acid, Pyrazinecarboxylic acid, 2,3-Pyrazinedicarboxylic acid and 2,2′-Bipyridine-4,4′-dicarboxylic acid. They were purchased from Sigma-Aldrich. $CoCl_2.6H_2O$, H_2SO_4, NaOH and *N,N*-dimethylformamide (DMF) were from Merck. Nitrogen (99.998%) and Oxygen (99.5%) were supplied by Indura S.A. (Argentina). Isopropyl alcohol was from Biopack. Nafion solution in isopropanol was purchased from Ion Power, Inc. (USA) (Liquion solution LQ1115 1100 EW 15%). Water was purified through an Arium Pro equipment from Sartorius until a specific conductivity of 18 MΩ cm^{-1}. Pt 20% supported on Vulcan XC-72 catalyst was obtained from ETEK.

2.2. Synthesis of MOFs and Coordination Polymers

In general, reported procedures were employed. In some cases, slight modifications described below were performed to increase the product yield or to avoid using organic solvents. Room temperature syntheses were preferred before solvothermal methods in order to obtain products with smaller particle sizes. The compounds have the prefixes 3D-, 1D- and 0D to clearly show that the precursor compounds are 3D-polymers (MOFs), 1D-polymers or a coordination compound or complex (0D).

3D-ZIF-67. A modification of the standard procedure (using Co $(NO_3)_2$ in organic solvent) was employed [21,22]. With this procedure the use of organic solvents was avoided and no traces of NO_3^- ions were present during the pyrolysis. Typically, 1.0 g of $CoCl_2.6H_2O$ were dissolved in 5 ml of water under Ar. 1.0 g of NaOH dissolved in minimum amount of water was added. The $Co(OH)_2$ thus formed was purified from Cl^- ions upon centrifugation and washing with Ar saturated water. To the pink suspension 3.0 g of 2-methylimidazole were added, affording a deep violet precipitate. This was stirred in an ultrasonic bath during one hour and allowed to completely react 24 hours. Finally the product was filtrated and air-dried. This deep violet MOF is composed of polyhedral particles ranging 500–1500 nm, similar to previous reports. The identity of the product was determined by powder XRD (CSD code GITTOT) [23].

3D-CoNic. 2 g of nicotinic acid and 2.5 g of Co $CoCl_2.6H_2O$ were dissolved in 6 mL of DMF. The deep blue solution was heated at 140 °C during 16 hs in a Teflon lined autoclave. The solvothermal synthesis afforded a dark red solid composed of highly dispersed (1–30 μm) irregularly shaped particles. The red solid was collected by filtration, washed with ethanol and air-dried. The product was identified by powder XRD (CSD code NERVEL) [24]. A synthesis in water (pH 6) was done producing a pink powder identified as a zwitterion complex through its powder XRD, not included in this study.

0D-$CoCO_2Pz$. 2.0 g of pyrazinecarboxylic acid were dissolved in 40 mL of a water solution containing 0.65 g ofNaOH. 1.9 g of $CoCl_2.6H_2O$ dissolved in 10 ml of water were added to the other solution, stirred some minutes and allowed to stand at room temperature 24 hs. An orange-yellow crystalline solid (1–10 μm particle size) was collected by filtration and air-dried. The identity of the product was determined by powder XRD (CSD code PRZCOC) [25].

1D-$Co(CO_2)_2Pz$. 2.0 g of 2,3-pyrazinedicarboxylic acid were dissolved in 40 mL of a water solution containing 0.95 g of NaOH. 2.8 g of $CoCl_2.6H_2O$ dissolved in 10 ml of water were added to the other solution, stirred some minutes and allowed to stand at room temperature 24 hs. The orange-yellow crystalline product, composed of 1–10 μm particles, was collected by filtration and dried air-dried. This compound was identified by powder XRD (CSD code TEBZAB) [26]. In the structure of this compound the $(CO_2)_2Pz$ ligands bridge Co^{2+} ions forming extended linear chains.

3D-Co(CO $_2$)$_2$bipy. 200 mg of 2,2′-Bipyridine-4,4′-dicarboxylic acid were dissolved in 5 mL of a water solution containing 70 mg of NaOH. 220 mg of $CoCl_2.6H_2O$ dissolved in 1 ml of water were added. The solution was transferred to a Teflon lined autoclave and heated at 140 °C during 48 hs. Afterwards, the fine orange-pink powder was collected by filtration and air-dried. The product was composed by microscopic needles (approximately $2 \times 25\ \mu m$) which exhibited very low dispersion in length and diameter. This MOF is a chiral interpenetrating 3-D coordination polymer constructed by different numbers of left- and right-handed helical chains. The product was identified by powder XRD (CSD code RAKBIO) [27].

2.3. Characterization of MOFs and Coordination Polymers

XRD. Powder X-ray diffraction patterns were measured using an Empyrean diffractometer equipped with a PixCel 3D detector, CuKα 40mA 40Kv radiation source, and with angle range $7° < 2\theta < 90°$, employing a 0.02° step size and a 4 s step time.

TGA. Thermogravimetric Analysis curves were recorded on a Shimadzu TGA 50, employing approximately 2.5 mg of sample, under a N_2 flow of 20 ml min^{-1} and a heating rate of 10 °C min^{-1}

2.4. Catalysts synthesis

Pyrolysis. Approximately 2.0 g of the precursor compounds were dried at 100 °C under N_2 during 2 hours. Then, they were submitted to pyrolysis at 700 °C or 900 °C during 2 hours, under Nitrogen (flow 1 l h^{-1}), using an Indef T300 tubular electric furnace at a heating rate of 10 °C min^{-1}.

Acid leaching. The raw products of the pyrolysis were treated with H_2SO_4 0.5 M at room temperature during 4 days. Each day the solid was separated using a centrifuge and fresh acid was added. Gas evolution was observed during the first day and the solution turned deep red. On the last day, the acid solution was colorless. This procedure was followed by washing with water until neutral pH, then with alcohol, and finally drying at 100 °C under reduced pressure during 24 hs. Stronger conditions (for example 100 °C) produced catalysts with lower ORR activity.

Ink preparation. 10 mg of the catalyst (previously grinded in an agate mortar) were suspended in 180 mg of isopropyl alcohol and set in the ultrasonic bath for 20 minutes. 30 μl of Nafion, (5% in isopropyl alcohol) were added and re-suspended. 10 μl of the ink thus prepared were spread on the 0.196 cm^2 gold disk, air-dried and employed in the electrochemical experiments.

2.5. Catalysts characterization

SEM/TEM/EDX. Catalyst morphology was characterized by Scanning Eelectron Microscopy (SEM) on a FEI Quanta 400 microscope or a Carl Zeiss NTS-SUPRA 40. Both instruments afforded the Energy-Dispersive X-ray spectra (EDX). Transmission Electron Microscopy (TEM) images were acquired with a Philips CM200 microscope.

Surface area and pore size distribution. A Micromeritics ASAP 2020 surface area and porosity analyzer was employ to determine the Brunauer-Emmett-Teller (BET) surface area and the Barret-Joyner-Halenda (BJH) pore diameter and volume distributions. Before measurements samples were degassed at 200 °C 8 hs at reduced pressure (10 mmHg).

XPS. X-ray photoelectron spectra were recorded under ultra-high vacuum conditions with a XPS SPECS spectrometer, using Mg Kα radiation, equipped with a 150 mm radius hemispherical electron energy analyzer and 20 eV pass energy. Binding energies were referred to the C 1s signal at 285 eV.

Raman. Spectra were recorded on a LabRAM HR Raman system (Horiba Jobin Yvon), equipped with two monochromator gratings and a charge coupled device detector. A 1800 g mm^{-1} grating and a 100 mm hole result in a spectral resolution of 1.5 cm^{-1}. The spectrograph is coupled to an imaging microscope with 10×, 50×, and 100× magnifications. The Ar laser line at 514.5 nm was used as excitation source and was filtered to give a laser power or density at the exit of the objective lens varying from 0.1 to 1 W mm^{-2}. Several measurements were performed, adjusting the laser fluence, to ensure that heating produced by the laser was minimized and that the sample was not altered. Measurements were taken in a backscattering geometry with a 50x magnification.

2.6. Electrochemical characterization

Electrochemical measurements. Electrochemical experiments were performed employing an Autolab PGSTAT302N potentiostat (Echochemie, Netherlands). For cyclic and linear sweep voltammetry experiments, the Autolab potentiostat was coupled to a RRDE (Rotating Ring Disc Electrode, 0.196 cm^2, Pine Research Inst.; Raleigh, NC). A Ag/AgCl (KCl saturated) reference electrode was used for all the electrochemical experiments and the potentials in this work were referred to the Reference Hydrogen Electrode (RHE), where $E(RHE) = E(Ag/AgCl) + 0.197V + 0.059pH$. The counter electrode was a large area rolled Platinum wire. A three electrodes electrochemical cell with a jacket was employed, and its temperature was kept at 25 ± 0.5 °C by circulating a thermostatized liquid using a Techne temperature controller.

Oxygen Reduction Reaction (ORR) experiments were performed in 0.5 M H_2SO_4 or 0.1 M KOH aqueous solutions. Linear sweep voltammograms were recorded at different rotation speed (ω = 100–2500 rpm). The potential was scanned at 5 mV s^{-1} between 1.1–0 V vs. RHE (acidic medium) and 1.4–0.2 V vs RHE (in alkaline medium), and the ring potential was fixed at 1.4 V vs. RHE (in acidic medium) and 1.6 V vs RHE (in alkaline medium) in order to oxidize the H_2O_2 generated in the disk. The calibration of the RRDE was carried out by measuring the disk and ring currents in a 0.005 M $K_3Fe(CN)_6$ + 0.1 M K_2SO_4 electrolyte, under identical conditions to those for ORR, affording N = 0.180 ± 0.005 [28].

Data analysis. Efficiency parameters, i.e. Tafel slopes, equilibrium potential (E_{eq}) and exchange current density (j_o) were calculated by means of Tafel plots (see Table 1) using the Nova 1.11 program. E_{eq} and j_o were determined from the intercept of the two trend lines corresponding to the ORR and the anodic process. j_o was calculated considering a geometrical area of the electrode, namely 0.196 cm^2. Errors in these parameters correspond to the standard deviation of several measurements, at least five.

The number of electrons transferred per molecule of reduced O_2, n_{e^-}, was determined through Koutecky–Levich plots (K-L). The overall measured current density, j, of the ORR can be expressed in terms of the kinetic current density, j_k, and the diffusion limited current density, j_d, by the Koutecky–Levich (K-L) equation (1) [28].

$$\frac{1}{j} = \frac{1}{j_k} + \frac{1}{j_d} = \frac{1}{j_k} + \frac{1}{B\omega^{1/2}} \quad (1)$$

$$B = 0.2 n_{e^-} F C_o D_o^{\ 2/3} \nu^{-1/6} \quad (2)$$

$$J_k = n_{e^-} F C_o k \quad (3)$$

In equations (2) and (3), 0.2 is a constant used when the rotation speed, ω, is expressed in rpm, F the Faraday constant (96485 A

$s\,mol^{-1}$), C_o is the concentration of dissolved oxygen (1.1×10^{-6} $mol\,cm^{-3}$), D_o is the diffusion coefficient of oxygen in the solution ($1.4\times10^{-5}\,cm^2\,s^{-1}$), ν referred as the kinematic viscosity of the 0.5 M H_2SO_4 solution ($1.0\times10^{-2}\,cm^{-2}\,s^{-1}$) and k is the electron transfer rate constant, all of them at 298 K. The inverse of the slope in the K-L plot, B, is proportional to n_{e^-}, and allowed to calculate this last parameter [28].

The yield in hydrogen peroxide, H_2O_2 can be calculated from equation (4)

$$\%H_2O_2 = \frac{200I_R/N}{I_D + I_R/N} \quad (4)$$

where I_R and I_D are the ring and the disk currents respectively, and N is the experimental collection efficiency (0.180 ± 0.005).

Cell Performance. Pt supported over Vulcan carbon (Pt/V) 20% w/w (E-Tek) was used as the anode catalyst, while the 1D-Co $(CO_2)_2Pz$ derived catalysts pyrolyzed at 700 °C, was used as cathode catalyst. The electrodes were prepared as follows. The catalyst suspension comprising approximately 100 mg catalyst with 70 mg isopropanol, 700 mg water and 400 mg Nafion ionomer solution (5% w/w, Ion Power), was spread on one side of a 5.0 cm^2 Toray C paper TGP–H 60 10% PTFE coated (Fuel Cell Technologies). The Pt catalyst loading was 5 mg, while the Co catalyst loading was 43 mg. A Nafion 212 membrane (Ion Power) was placed between the electrodes and then hot pressed at 140 °C and 50 bar for 25 min. The Nafion membrane was previously treated by boiling in H_2O_2 3% w/w (H_2O_2 30% w/w, Biopack) followed by H_2SO_4 3% w/w (95-97% w/w, Merck). Humidified H_2 (RG 4.8, Indura) and O_2 (RG 4.8, Indura) were circulated at the anode and cathode, respectively, at different flow rates. Galvanodynamic polarization tests were performed at 80 °C. The measurements were performed using a University Test Station system from Fuel Cell Technologies.

3. Results and discussion

In order to evaluate the influence of the precursor structure on the N-doped carbon activity towards ORR, several Cobalt MOFs, a coordination polymer and a complex were synthesized. The following N-heterocyclic ligands were employed: 2-Methylimidazole (for ZIF-67) [21–23], nicotinate (Nic) [24], pyrazinecarboxylate (CO_2Pz) [25], 2,3-pyrazinedicarboxylate ($(CO_2)_2Pz$) [26] and 2,2′-bipyridine-4,4′-dicarboxylate ($(CO_2)_2$bipy) [27]. These ligands were chosen aiming to maximize formation of CoN_4 sites and

Table 1
Relevant physical and electrokinetic parameters from N-doped carbons and related compounds.

Catalyst [a]	BET area ($m^2\,g^{-1}$)[b]	Mesoporous area ($m^2\,g^{-1}$)[c]	Co atom %[d]	N atom %[d]	Tafel slope (mV dec^{-1})[e]	j_o ($\mu A\,cm^{-2}$)[e,f]	E_{eq} (mV vs RHE)[e]	$E_{1/2}$ (mV vs RHE)[g]	n_{e^-}[h]	% H_2O_2[i]
3D-ZIF-67 700 °C	447 ± 5	100 ± 20	12 ± 4	6.1 ± 0.2	81 ± 9	25 ± 5	901 ± 30	700 ± 10, 710[j]	3.9–4.0	3–9
3D-ZIF-67 900 °C	462 ± 5	240 ± 20	2.2 ± 0.2	1.9 ± 0.2	79 ± 3	10 ± 2	880 ± 10	690 ± 10, 710[j]	3.5–3.8	8–15
1D-Co$(CO_2)_2Pz$ 700	320 ± 5	230 ± 20	12 ± 8	3.3 ± 0.9	82 ± 9	10 ± 3	907 ± 30	720 ± 10	3.6–4.0	7–10
1D-Co$(CO_2)_2Pz$ 900 °C	394 ± 5	400 ± 20	0.8 ± 0.2	1.7 ± 0.7	83 ± 9	9 ± 3	905 ± 20	700 ± 20	3.6–3.9	12–20
3D-CoNic 700 °C	408 ± 5	266 ± 7	2.4 ± 0.3	3.1 ± 0.5	81 ± 2	12 ± 4	900 ± 20	650 ± 20	3.7–4.0	3–14
3D-CoNic 900 °C	391 ± 5	290 ± 7	2.5 ± 1	2.0 ± 0.6	81 ± 3	7 ± 2	902 ± 10	670 ± 10	3.8–4.0	9–21
3D-Co $(CO_2)_2$bipy700 °C	309 ± 5	183 ± 7	2.6 ± 0.4	2.1 ± 0.3	83 ± 5	9 ± 5	924 ± 2	610 ± 40	3.4–4.0	15–23
3D-Co $(CO_2)_2$bipy900 °C	338 ± 5	240 ± 10	0.7 ± 0.2	2.0 ± 0.2	81 ± 6	9 ± 2	913 ± 10	700 ± 3	3.6–3.9	20–33
0D-CoCO_2Pz 700 °C	400 ± 5	228 ± 7	6 ± 2	2.1 ± 0.5	92 ± 1	9 ± 3	926 ± 2	580 ± 30	3.0–3.5	10–17
0D-CoCO_2Pz 900 °C	307 ± 5	202 ± 7	0.7 ± 0.3	2.0 ± 0.2	73 ± 2	5 ± 1	910 ± 8	650 ± 30	2.8–3.8	13–30
PANI-Fe-C [k]					87		920	810	4.0	*ca* 1
ZIF-67/ZIF-8 [l]	1563		0.80	6.19			930	760	3.7–3.8	15
Fe-ZIF-8 [m]	969		3.3(Fe)	6.9	70		950	820	3.98	<1
Fe(phen)-ZIF-8 [n]	954	184	0.8	5.3			980	880		
Co(phen) x2 meso[o]					90 ± 5	25 ± 2	900 ± 10	720	4.0–4.1	5–9
Pt 20% vulcan [o]					85 ± 7	60 ± 8	990 ± 2	830	3.9–4.1	0.5–1

[k-l] The onset-potential is reported instead of the equilibrium potential (E_{eq}).
[a] For data analysis and catalysts synthesis, see experimental section. Electrochemical data corresponds to 0.5 M H_2SO_4 otherwise stated.
[b] From N_2 adsoprtion- desorption experiments.
[c] From BJH adsorption cumulative surface area of pores 2–50 nm width.
[d] From EDX.
[e] From Tafel plots, see experimental section.
[f] j_o was calculated considering the geometrical area of the electrode (0.196 cm^2).
[g] From steady-state ORR polarization curves (see SI).
[h] Koutecky-Levich plots (see SI).
[i] From RRDE experiments obtained at 2500 rpm(see SI).
[j] From references [21] and [22].
[k] From reference [45].
[l] Electrochemistry measured at 0.1 M $HClO_4$, from reference [53].
[m] Electrochemistry measured at 0.1 M $HClO_4$, from reference [56].
[n] for N and Fe contents and surface areas see reference [56]; electrochemistry measured at 0.1 M H_2SO_4, from reference [9].
[o] From reference [34].

pyridinic N atoms on the carbon surface after pyrolysis. Powder XRD patterns of the precursors (see Supplementary Information, SI, Figure SI1) reproduced those simulated from reported crystal structures.

3.1. Physical characterization

The thermal properties of the precursor compounds were characterized by **TGA** (Figure SI 2). In general there was an initial weight loss of 5–10% between 120–220 °C which corresponded to the release of coordinated water molecules or solvent absorbed within the pores. A second, more pronounced process was observed between 300–600 °C which involved ligand volatilization, reaction of functional groups, decarboxylation of carboxylic groups, ligand condensation, etc. [29,30]. Graphitization occurred at temperatures higher than 700 °C as evidenced by Raman spectroscopy and XRD patterns of the pyrolysis products (*vide infra*). Co^{2+} ions were partially reduced, generating metallic particles, as detected by XRD and TEM [29]. From the TGA, ZIF-67 MOF exhibited the highest weight after thermal treatment between 600–900 °C. This could be ascribed to the lack of carboxylate groups in the ligand, (which are eliminated as gaseous CO_2), and to the tri-dimensional structure, which may confer additional stability. The 1D polymer, $Co(CO_2)_2Pz$, had the second mass retention after ZIF-67, probably due to the stability associated to the chelating structure of the $(CO_2)_2Pz$ ligand. The CoNic MOF has labile carboxylate groups and no chelating ligands, what located this compound in the middle of the series. Surprisingly, the $Co(CO_2)_2$bipy compound, a 3D MOF, with the chelating bipyridyl group, had the second lowest weight retention after pyrolysis. Finally, the $CoCO_2Pz$ complex showed the lowest weight after pyrolysis. This trend will be discussed in relation with ORR activity.

All the precursors generated powder samples after pyrolysis, with the exception of $CoCO_2Pz$ complex. This compound could

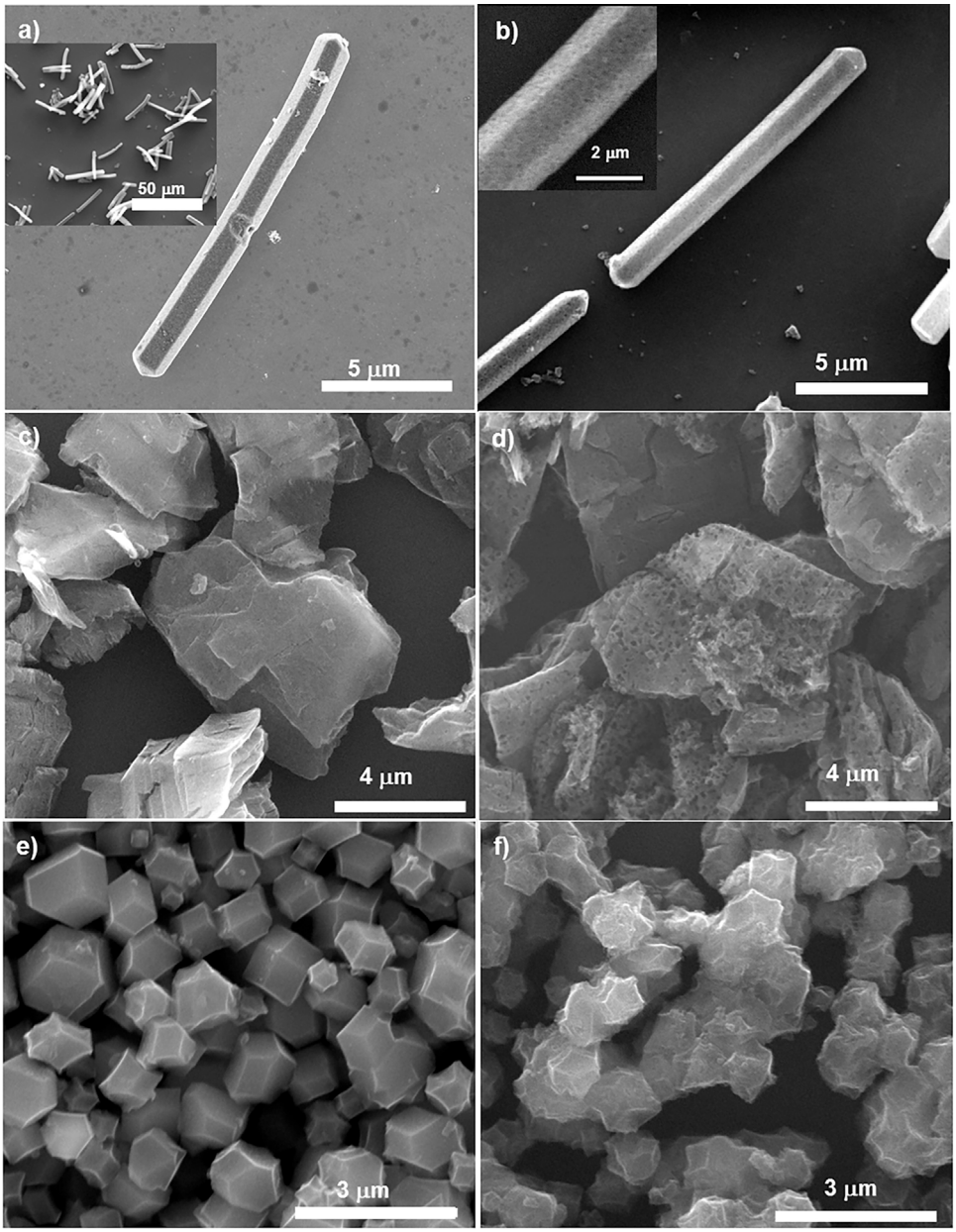

Fig. 1. a), b) SEM images of the 3D-$Co(CO_2)_2$bipy derived carbons obtained at 700 °C (a) and 900 °C (b). **c,d)** SEM images of the 1D-$Co(CO_2)_2Pz$ derived samples obtained at 700 °C (c) and 900 °C (d). **e,f)** SEM images of the 3D-ZIF-67 derived catalysts obtained at 700 °C (e) and 900 °C (f).

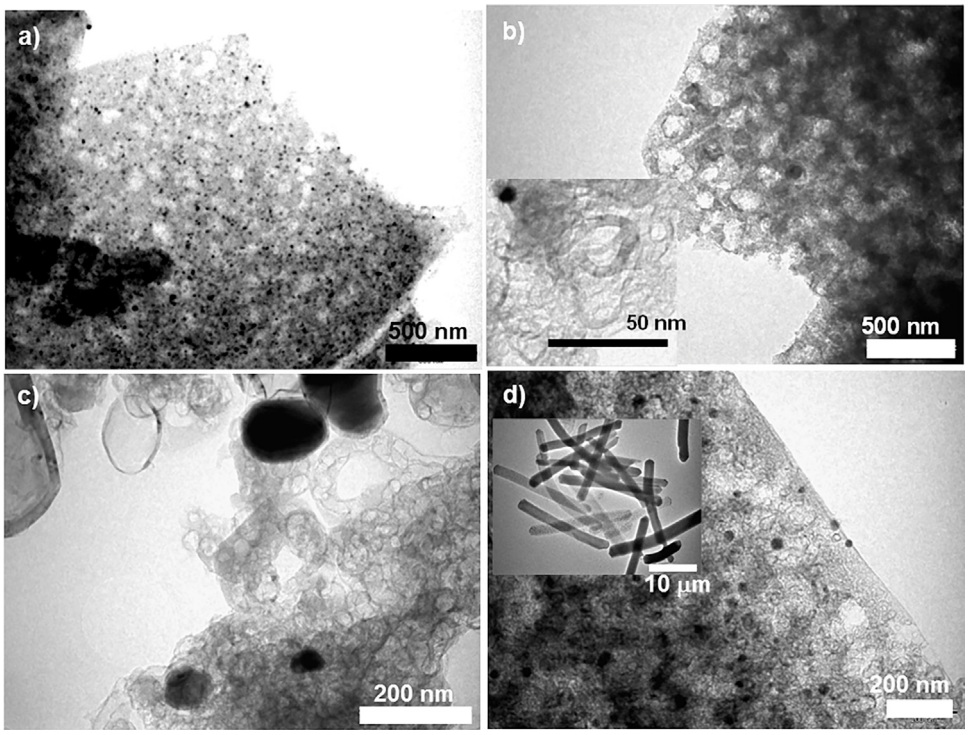

Fig. 2. a,b) TEM images of the 1D-Co$(CO_2)_2$Pz derived carbons obtained at 700 °C (a) and 900 °C (b), inset higher magnification image. **c)** TEM image of the 3D-CoNic derived catalyst obtained at 900 °C. **d)** TEM image of the 3D-Co$(CO_2)_2$bipy derived sample obtained at 900 °C, inset lower magnification image.

afford a monolithic material if the starting compound was pressed as a cake or pellet before pyrolysis (see Figure SI 4).

Figs. 1 and 2 show **SEM and TEM** images of selected catalysts obtained at 700 °C – 900 °C and leached with 0.5 M H_2SO_4. SEM images of the precursor compounds and other pyrolyzed samples are shown in the SI. External morphology of the particles was kept during the thermal and acid treatment. Macropores of approximately 100 nm could be observed in most of the materials pyrolyzed at 900 °C, what made the particles look like sponges (see Figs. 1b, d and 2). This also held for the 3D-CoNic and 1D-Co$(CO_2)_2$Pz pyrolyzed at 700 °C (2a and SI). However, the 3D-ZIF-67 and 0D-CoCO_2Pz derived samples (700 °C) did not show such features under the magnification employed (Figs. 1e and SI). TEM images of selected samples exhibited dark particles embedded within the carbon matrix identified as Co nanoparticles through the EDX spectra (Fig. 2), in agreement with XRD data (SI). For the 1D-Co$(CO_2)_2$Pz derived materials, these nanoparticles had a diameter of ca 20 nm (700 °C) and 75 nm (900 °C) (see Fig. 2a, b). Similar picture has been reported for 3D-ZIF-67 derived catalysts [21,22]. This was also observed for 3D-Co$(CO_2)_2$bipy (900 °C) exhibiting Co particles of approximately 35 nm (Fig. 2d). A different situation was observed with 3D-CoNic. In this case, large particles (30 μm, Figure SI 4) were composed of smaller particles of carbon (ca 50 nm, Fig. 2c) and metallic particles (ca 120 nm, Fig. 2c) covered or encapsulated by carbon.

XRD studies performed on the pyrolysis products of the Co compounds leached with 0.5 M H_2SO_4 (Figure SI 5) revealed the presence of diffraction peaks assignable to reflections of the (111) and (200) planes in metallic Co [30]. A shoulder at 42.5° observed in some samples can be ascribed to the (200) reflection of CoO. Samples obtained at 900 °C displayed a signal at 26.2° which corresponds to the (002) reflection in graphite [30]. This signal had lower intensity in samples obtained at 700 °C. This last result is consistent with the lower degree of graphitization observed by Raman spectroscopy in the 1D-Co$(CO_2)_2$Pz 700 °C sample.

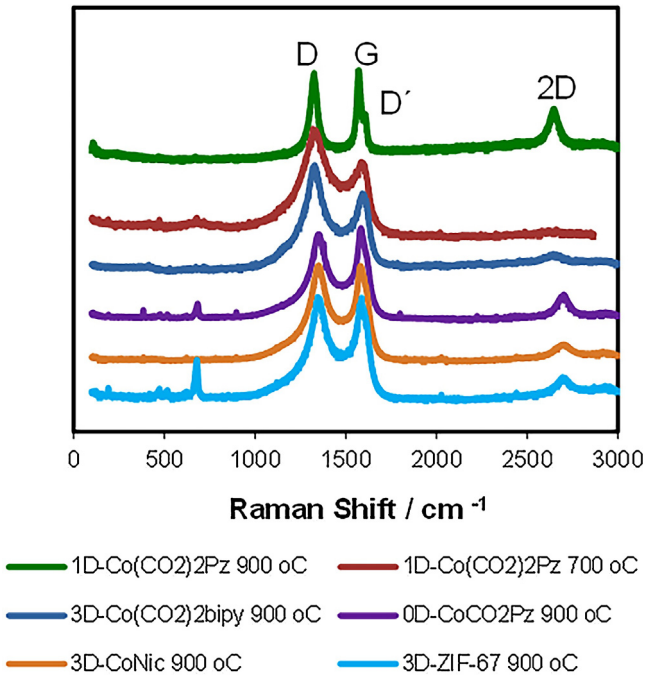

Fig. 3. Raman spectra of selected catalysts.

Some selected samples were studied through **Raman** spectroscopy. The spectra of the pyrolyzed samples (700 and 900 °C, leached with 0.5 M H_2SO_4), showed in Fig. 3, are dominated by two bands at *ca* 1330 cm^{-1} and *ca* 1590 cm^{-1}. The first signal, called D band, is present in all graphite-like carbons and originates from structural defects and sp^3 carbons [31]. The second signal, called G band, is assigned to the E_{2g} stretching vibrations in the basal plane of graphite [31]. The 1D-Co$(CO_2)_2$Pz 700 °C sample (compared with

the one obtained at 900 °C), displayed a lower relative intensity of the G band (compared to the D band) consistent with a lower degree of graphitization at this lower temperature. This is consistent with the powder XRD results. The D' band (1610 cm^{-1}) is also caused by disorder and defects [31]. The 2D band at 2700 cm^{-1}, a second-order two-phonon process, is typical of carbon nanotubes or graphene sheets. Nanotube formation has been directly observed by TEM and SEM in 3D-ZIF-67 pyrolyzed samples [32]. Other signals at 190 cm^{-1}, 472 cm^{-1}, 515 cm^{-1}, 610 cm^{-1} and 680 cm^{-1} were also present in the spectra (Fig. 3). Based on literature data, they can be assigned to CoO or to a mixture of CoO/Co_3O_4 [33,34]. The presence of CoO was also detected with low intensity in some XRD patterns of the pyrolysis products (see SI).

Pyrolyzed acid leached samples were studied by **EDX** spectroscopy to determine their composition. In Table 1, N and Co contents (atom %) are summarized (C, O and S data are shown in the SI). Both parameters decreased at 900 °C compared to 700 °C. The reduction in Co content could be understood in terms of the dynamics of Co particle formation, with consequent pore and channel generation [22]. They must facilitate the acid penetration and particle dissolution. N content also decreased drastically as the pyrolysis temperature increased, in agreement with previous results and XPS data [21,22]. The data for Co content exhibited a much higher dispersion than the corresponding values for N content, probably due to the heterogeneity caused by the metallic particles, observed by SEM and TEM.

The pyrolysis products of the 0D-$CoCO_2Pz$ complex obtained at 700 °C and 900 °C (leached with 0.5 M H_2SO_4) were studied through **XPS**. The survey spectra exhibited features assignable to the C 1s, N 1s, O 1s, Co 2p core levels (See Figure SI 6). The high resolution N 1s spectra could be deconvoluted into four subspectra centered at 398.5 eV, 399.6 eV, 401.0 eV and 403.0 eV (see Fig. 4), which were ascribed, according to literature, to Pydinic N (397–399 eV), Co coordinated N (399–400 eV), Graphitic N (401- 402 eV), and Oxidized N (402–405 eV), respectively [35–37]. Pyridinic-N refers to the nitrogen atom on the edge of a graphite plane with two adjacent carbon atoms. It has one lone pair of electrons in addition to the electron donated to the conjugated bond system, imparting Lewis basicity to the carbon. Co coordinated N also corresponds to a Pyridinic N atom, but coordinated to Co instead of being free. Graphitic-N, which is also termed as "Quaternary-N", represents the nitrogen atom bonded to three carbon atoms within a graphite (basal) plane, while Pyrrolic groups (400–401 eV) refer to nitrogen atoms that contribute to the π system with two π electron within a five-membered ring. Finally, Oxidized-N corresponds to N bound to O (N^+-O^-) [35,36]. From these spectra, it was not possible to distinguish or resolve Pyrrolic N from Graphitic N. Upon thermal treatment at 900 °C the intensities of the total N decreased, Co coordinated N signals were not detected and the Graphitic N increased its relative intensity compared with Pyridinic N. These spectra, employing a pyrazine derived ligand, were very similar to the ones previously found on 3D-ZIF-67 pyrolysis products, with methylimidazole as ligand [21,22,38]. This result is relevant to ORR since Pyridinic and CoN_4 groups have been postulated as the active sites where O_2 reduction takes place [7–10].

The XPS spectra in the region of the Co 2p binding energy of the 0D-$CoCO_2Pz$ complex pyrolyzed at 700 °C displayed signals centered at 780.5, 795.7, 785.3 and 802.8 eV (see Fig. 4). This is a fingerprint for the presence of Co(II) high spin ions [39–41]. For the CoO compound, the Co $2p_{3/2}$ binding energy is reported to be at 780.0–780.9 eV and its Co $2p_{1/2}$ spin orbit coupling component at 796.0–796.5 eV [39–41]. The CoO is characterized by two shake up satellites reported at 785.3 and 802.6 eV [39–41]. The spectrum of the 0D-$CoCO_2Pz$ complex pyrolyzed at 700 °C closely resembled

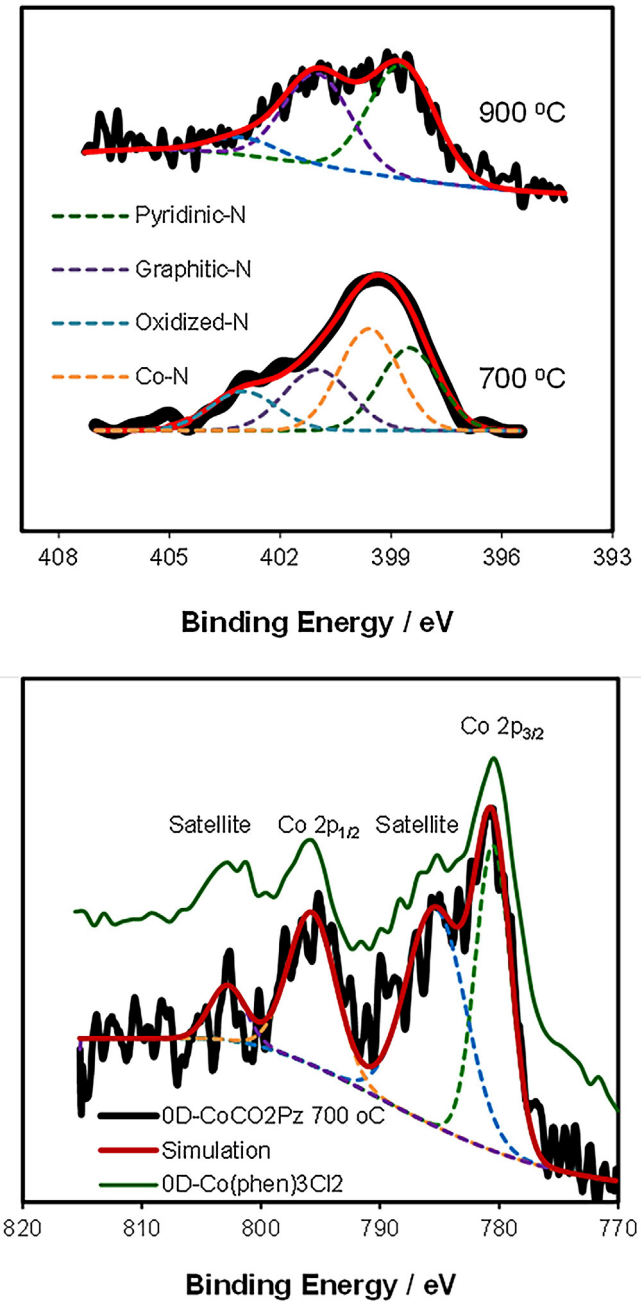

Fig. 4. High resolution XPS spectra corresponding to the N 1s and Co 2p core levels of the 0D-$CoCO_2Pz$ compound pyrolyzed at 700 °C and 900 °C (0.5 M H_2SO_4 leached), experimental spectra (black bold lines), subspectra (dotted lines, see text) and total simulations (red line). Co 2P spectrum of $[Co(II)(phen)_3]Cl_2$ complex (not pyrolyzed) is show for comparison.

that of the $[Co(II)(phen)_3]Cl_2$ complex (not pyrolyzed). In this way, the Co(II) centers could be partially coordinated to Pyridinic-N as observed in the N 1S spectrum. The absence of a subspectrum centered at 778 eV indicated that Co metallic particles (detected by powder X-ray diffraction) must be covered by CoO, or encapsulated by carbon (as seen by TEM), thus, not detectable by XPS which is selective to the first atomic layers. Co_3O_4 shows much weaker satellite signals, and 2p binding energies at 779.5–780.7 and 794.5–795.3 eV for the $2p_{3/2}$ and $2p_{1/2}$ core levels respectively [39–41], with satellites 787.9 and 803.0 eV. Finally, the 0D-$CoCO_2Pz$ pyrolyzed at 900 °C sample, did not show detectable signals of Co,

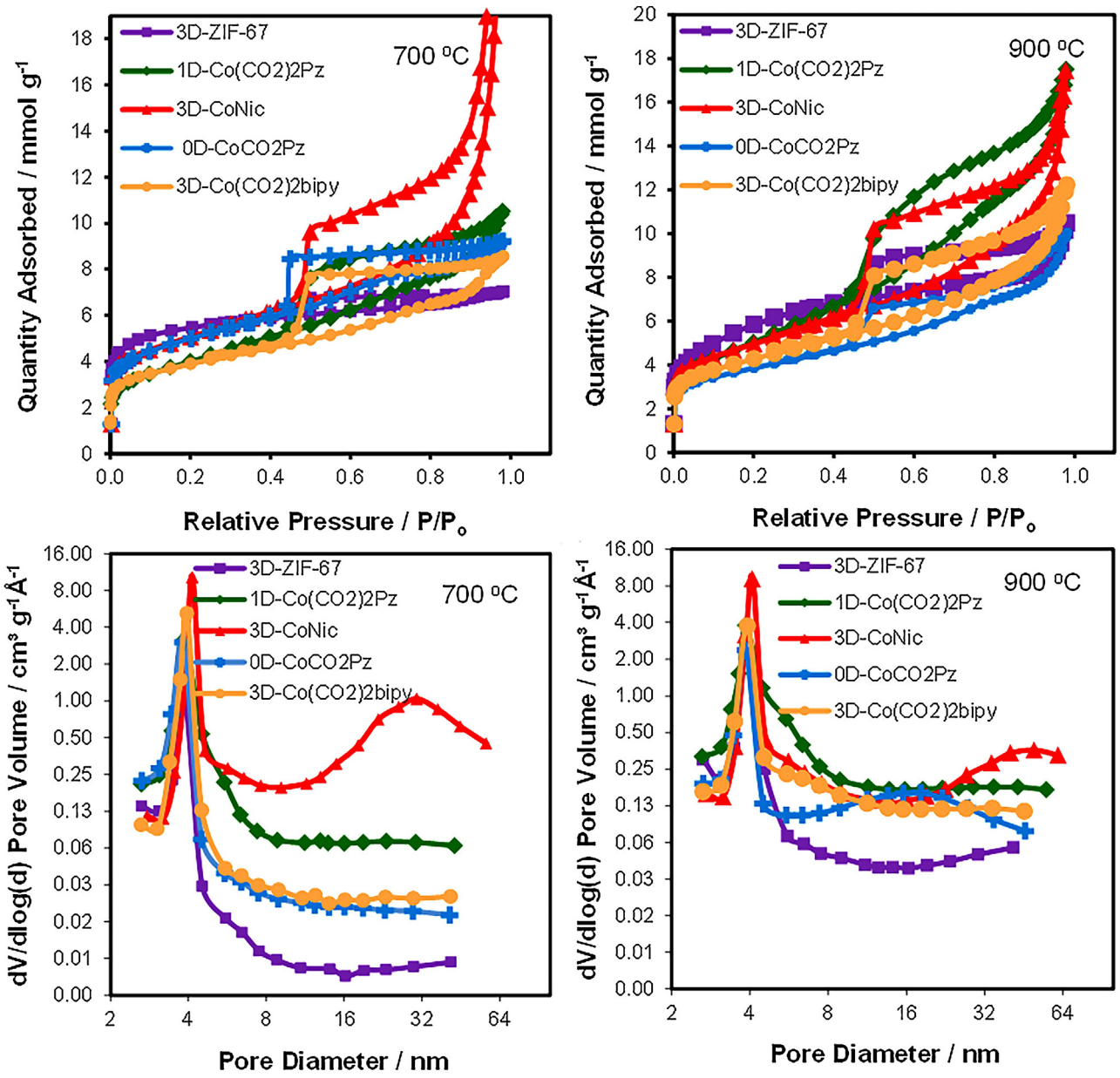

Fig. 5. Top: N_2 adsorption/desorption isotherms at 77 °K for the prepared catalysts. Bottom: Pore size distributions obtained from the BJH Desorption dV/dlog(d) Pore Volume vs Pore Diameter plots.

in agreement with its lower metal content detected by EDX and the absence of Co-N signals in the N 1S XPS.

The **surface area and pore size distributions** of the prepared catalysts were investigated through N_2 adsorption–desorption measurements at 77 K. Fig. 5 shows the isotherms for the materials prepared at 700 °C and 900 °C. They exhibit typical Type IV isotherms according to IUPAC classification [42]. The steep increase of N_2 uptake at low pressure and hysteresis loop at high pressure are characteristics of micro- and meso-porous structures respectively [30,42]. BET surface areas took values between 300–460 $m^2\,g^{-1}$ (see Table 1). In most cases these parameters increased with pyrolysis temperature, in agreement with previous reports [22]. Both, pyrolysis and acid leaching have deep effects on the surface area and pore size distribution. During pyrolysis the microporous structure of the MOF collapses. On the other hand Co nanoparticle formation at expenses of smaller ones and Co^{2+} ions, leaving empty pores and channels, contributes to the mesopore formation. These particles are partially dissolved during acid leaching, generating pores as well. As an example, the 3D-ZIF-67 derived catalysts showed a BET surface area of 447 and 462 $m^2\,g^{-1}$ (at 700 °C and 900 °C respectively, Table 1), in very good agreement with the reported value of 501 $m^2\,g^{-1}$ (900 °C, acid leached) [22]. In contrast a BET surface area of 285.9 and 258 $m^2\,g^{-1}$ has been reported for 3D-ZIF-67 pyrolyzed at 900 and 700 °C respectively, without acid leaching [22]. The precursor compound (ZIF-67) has a reported BET surface area of 1512 $m^2\,g^{-1}$ [21]. On the other hand, the 1D-Co$(CO_2)_2$Pz derived catalysts showed smaller BET surface area of 394 and 320 $m^2\,g^{-1}$ (900 and 700 °C respectively).

The area on mesopores (2–50 nm) was approximately 60% (700 °C) – 70% (900 °C) of the BET surface area, for most of the

samples (see Table 1). However, for the 3D-ZIF-67 (700 °C) sample, the area on mesopores was only 23% of the BET area. In contrast, for the 1D-Co$(CO_2)_2$Pz derived catalyst, the area on mesopores reached 80% (700 °C) and *ca* 100% (900 °C) of the BET surface area. The micropore area ranged 40–80 $m^2 g^{-1}$ for all the samples, except for the ZIF-67 700 °C material, which exhibited a much higher value of 220 $m^2 g^{-1}$. A relation between the area on mesopores and the activity for ORR will be discussed in the last section.

The pore size distributions obtained from the BJH desorption dA/dlog(d) Pore Area plots showed a narrow peak centered at 3.8–4.1 nm (see Fig. 5), and the presence of larger pores, depending of the sample. This was particularly evident for the 1D-Co$(CO_2)_2$Pz and 3D-CoNic derived materials. Remarkably, the 3D-CoNic samples exhibited the presence of a second maximum in both distributions plots (see Fig. 5) at 30 nm (700 °C) and 50 nm (900 °C), i.e. a bimodal, hierarchical pore size distribution. In contrast the 3D-ZIF-67 derived catalysts showed a very narrow distribution of pores after both thermal treatments.

It is worth noting that the surface areas and pore distributions did not change if the sample was a powder or a monolith, and did not depend on the grinding of the samples. This evidenced that these properties were dominated by the micro- or mesoporosity and not by the external surface in these relatively large particle samples. For 3D-ZIF-67 (750 °C) samples (not acid leached) the BET surface areas were reported to be 386 $m^2 g^{-1}$ (300 nm), 326 $m^2 g^{-1}$ (800 nm), 233 $m^2 g^{-1}$ (1.7 μm) and 165 $m^2 g^{-1}$ (bulk) [21]. In these cases the pores were probably occupied by Co/CoO particles.

3.2. Electrochemical characterization

The activity of the Oxygen Reduction Reaction (ORR) was studied employing linear sweep voltammetry on a rotating ring-disk electrode (RRDE) in O_2–saturated 0.5 M H_2SO_4 and 0.1 M KOH solutions. The steady-state polarization curves (I vs V) are shown in the SI for the different samples under different rotation speeds. The curves obtained at 2500 rpm are shown in Fig. 6. Tafel plots (0.5 M H_2SO_4) afforded the electrokinetic parameters, which are shown in

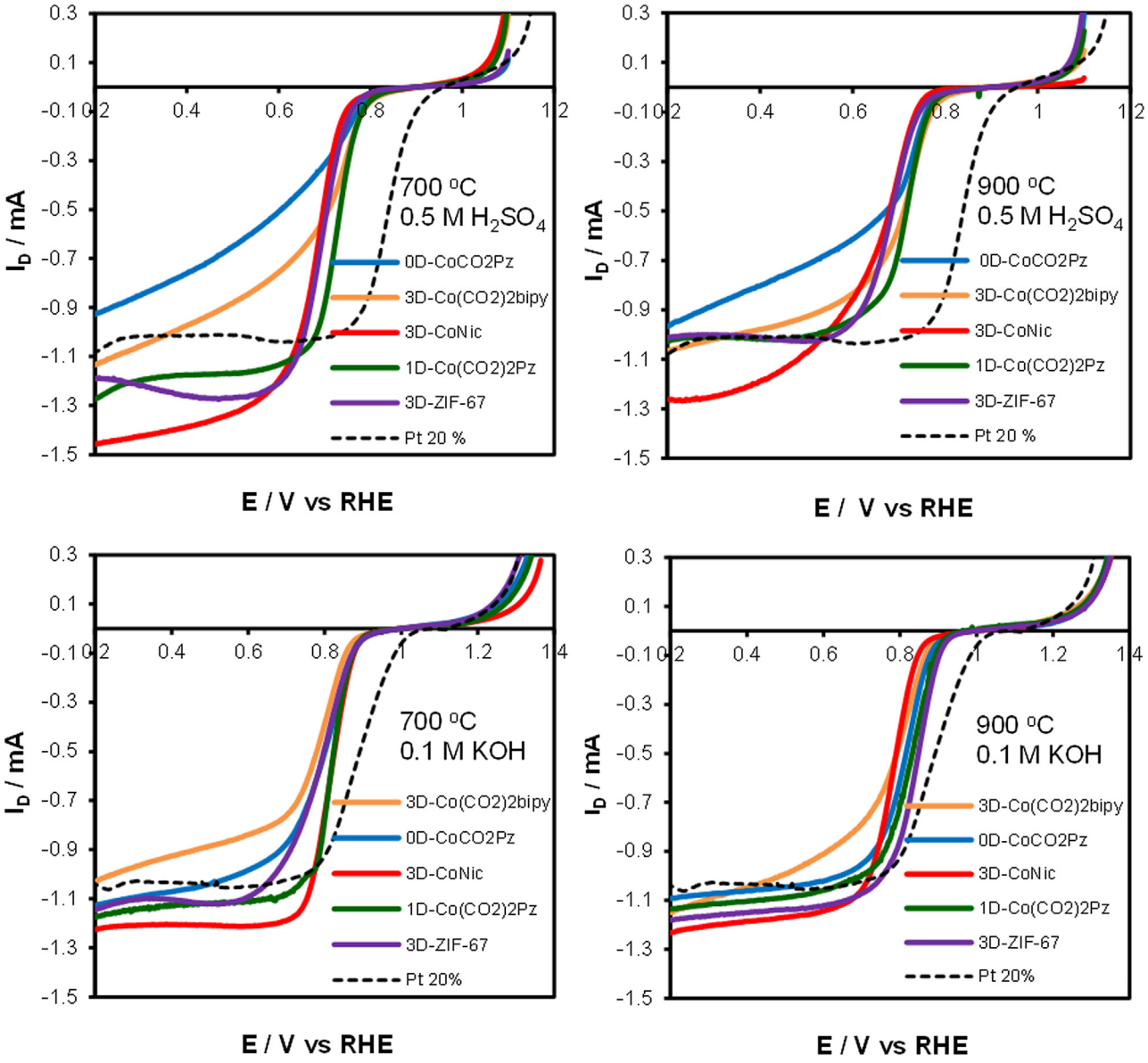

Fig. 6. Top: Current–potential curves on the catalysts obtained at 700 and 900 °C in an O_2-saturead 0.5 M H_2SO_4 solution on Au disk at 2500 rpm at 25 °C. Bottom: Current–potential curves on the catalysts obtained at 700 and 900 °C in an O_2-saturead 0.1 M KOH solution on Au disk at 2500 rpm at 25 °C.

Table 1. The Tafel slope and the equilibrium potential (E_{eq}) took approximately the values 80 ± 10 mV dec^{-1} and 900 ± 20 V vs RHE respectively for all the samples. This was consistent with the presence of similar active sites in all the catalysts. The 3D-ZIF-67 700 °C sample displayed the highest exchange current density (j_o) of 25 μA cm^{-2}, what could be ascribed to both the higher surface area, and higher Co and N contents (see Table 1). The other samples exhibit a j_o around 9 μA cm^{-2}. However, the current intensities at lower potentials (< 0.5 V), i.e. limiting currents, were different, taking particularly lower values for the 0D-$CoCO_2Pz$ and 3D-Co$(CO_2)_2$bipy derived samples (at both thermal treatments). A possible explanation will be offered in the next Section (3.3).

All the samples pyrolyzed at 900 °C showed a significantly higher % H_2O_2 yield than the ones obtained at 700 °C. This could be related to the lower N and Co contents detected in the former samples, what could support the relevant role of both types of atoms (most probably as CoN_4 species) in the reduction of H_2O_2, or O_2 directly to H_2O. Koutecky-Levich plots are shown in the SI. The numbers of exchanged electrons (n_{e^-}) obtained from these plots are listed in Table 1 and they had reasonable agreement with the H_2O_2 yield, supporting a 4 e^- reduction mechanism. Although the proposed mechanisms for ORR include several steps, they follow basically two routes: a direct reduction of O_2 to H_2O (4 e^-) or a reduction of O_2 to H_2O_2 (2 e^-) [43]. Eventually, H_2O_2 can be further reduced to H_2O, can dismutate, or can be released to the solution as by product, with consequent reduction in power generation and corrosive effects towards different parts of the PEM-FC. Many different species are present on the surface of Fe- or Co-N-doped carbons and several of them have been proposed as active sites [7–10]. An electrochemical and spectroscopic study performed by Artyushkova et al., concluded that Pyrrolic N catalyzes the first step of O_2 reduction to H_2O_2 [7,10]. Pyridinic N serves as a second step of H_2O_2 reduction to water. Metal coordinated to N catalyzes the 4e^- direct reduction of O_2 to water and/or the second step of H_2O_2 reduction similarly to the Pyridinic N [7,10]. In agreement with these findings, samples obtained at 700 °C with higher Co and N content, particularly Co-coordinated N (as detected in 0D-$CoCO_2Pz$ 700 °C by XPS) exhibited significantly lower H_2O_2 yields and number of exchanged electros closer to 4 (see Table 1).

Finally, these catalysts were studied in alkaline medium (0.1 M KOH) (see Fig. 6, bottom). Non Platinum group catalysts usually exhibit better performance in this medium [12,18]. In our case, voltammograms closely resembled those obtained in acidic medium but with potential shifted towards more positive potentials. Particularly half wave potentials ($E_{1/2}$) and diffusion limiting currents were close to those of Pt 20% supported on carbon. The limiting currents were further improved upon thermal treatment at 900 °C. Differences in the performances in acid and basic media can be ascribed to differences in the optimal active sites in both electrolytes. FeN_x and CoN_x are more active in acid medium, while Pyridinic N and Graphitic N are apparently more active in basic solution [10,11].

A preliminary test was performed with the 1D-Co$(CO_2)_2$Pz 700 °C derived catalyst as cathode in single-cell acidic PEM fuel cell. This measurement will be improved in the near future and is shown in Figure SI 14. It exhibited a peak power of 60 mW cm^{-2}. This sample showed higher methanol tolerance than Pt 20% (0.05 M methanol, 0.5 M H_2SO_4 see Fig. 8). Finally, the same catalyst did not show any detectable change in ORR activity after 3000 cycles between 0.25–1.15 V vs RHE (O_2 saturated 0.5 M H_2SO_4, see Fig. 8).

3.3. Activity vs structure correlation

Although all the samples showed a similar j_o around 9 μA cm^{-2} (0.5 M H_2SO_4, except 3D-ZIF-67 700 °C, j_o = 25 μA cm^{-2}), their current intensities at lower potentials (< 0.5 V), i.e. the diffusion limited currents, were different (see Fig. 6). A possible explanation can be met if the surface on mesopores is analyzed (Table 1). Fig. 7 shows a plot of the disk intensity (I_D, at 0.5 V vs RHE, 0.5 M H_2SO_4) vs the mesopore area occupied by N atoms (% N x surface on mesopores). Although with high dispersion, a correlation can be observed between both parameters for all the data. The analogous plot for Co is shown in the SI. The 3D-ZIF-67 700 °C sample had the highest nitrogen content (6.1%), highest BET surface area (447 m^2 g^{-1}) and highest micropore area (220 m^2 g^{-1}) as well. On the other hand, the 1D-Co$(CO_2)_2$Pz 700 °C catalyst had one of the lowest BET surface area (320 m^2 g^{-1}) and 3.3% N content (see Table 1). However, their linear sweep voltammograms were very similar (see Fig. 6). In contrast, the 3D-ZIF-67 700 °C material held the lowest surface on mesopores (2–50 nm) (see Table 1, 100 m^2 g^{-1}), while for the 1D-Co$(CO_2)_2$Pz 700 °C sample this parameter took the value 230 m^2 g^{-1}. This would compensate, at least partially, the higher surface area and N content of the first compound. Based on experimental and geometrical considerations, micropores (< 2 nm) have been proposed as crucial for catalytic activity, since the distance between two micropore walls should have an exact value (1–2 nm) for the active site M-N_x to be formed [44,45]. However, micropores are less accessible to solvent, and may control the diffusion process when the electron transfer reaction is faster, at lower redox potentials (diffusion limiting regime). Macro- and mesopores are needed for fast mass transport especially at high current rates [18,32,46,47]. A proper combination of both micropores and mesopores is necessary for a good performance of the catalysts [48]. The plot I_D vs % Co x surface on mesopores is shown in the SI. No correlation or trend could be observed. This could be attributed to the presence of significant amounts of Co metallic particles encapsulated within the carbon matrix, which are not active for ORR, but detected by EDX. Co species were not detected by XPS in the 0D-$CoCO_2Pz$ 900 °C sample, however, it still showed ORR activity (with high H_2O_2 yield). This means that other species, like Pyridinic N are also responsible for the ORR, in addition to Co-N_4, which was detected in the sample pyrolized at 700 °C [7].

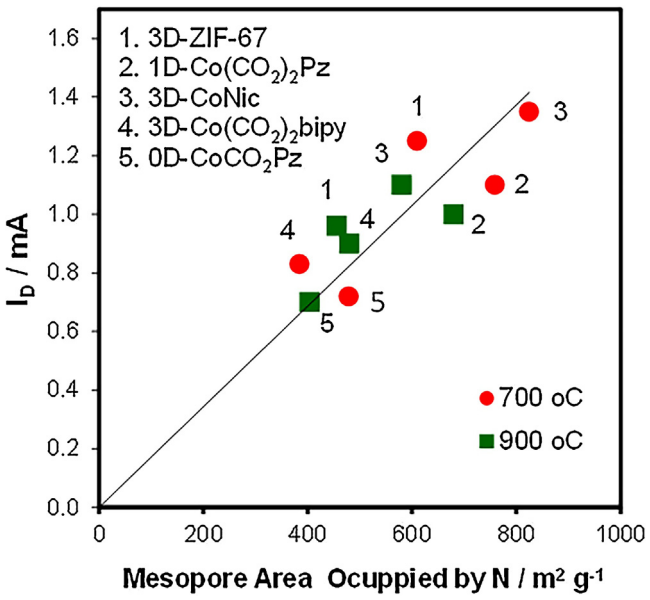

Fig. 7. Plot for the disk intensity vs mesopore area occupied by N atoms (% N x area on mesopores). Area on mesopores corresponds to BJH Adsorption cumulative volume of pores between 2–50 nm width). Disk intensity (at 0.5 V vs RHE, O_2 saturated 0.5 M H_2SO_4), corresponds to the average of at least four independent measurements.

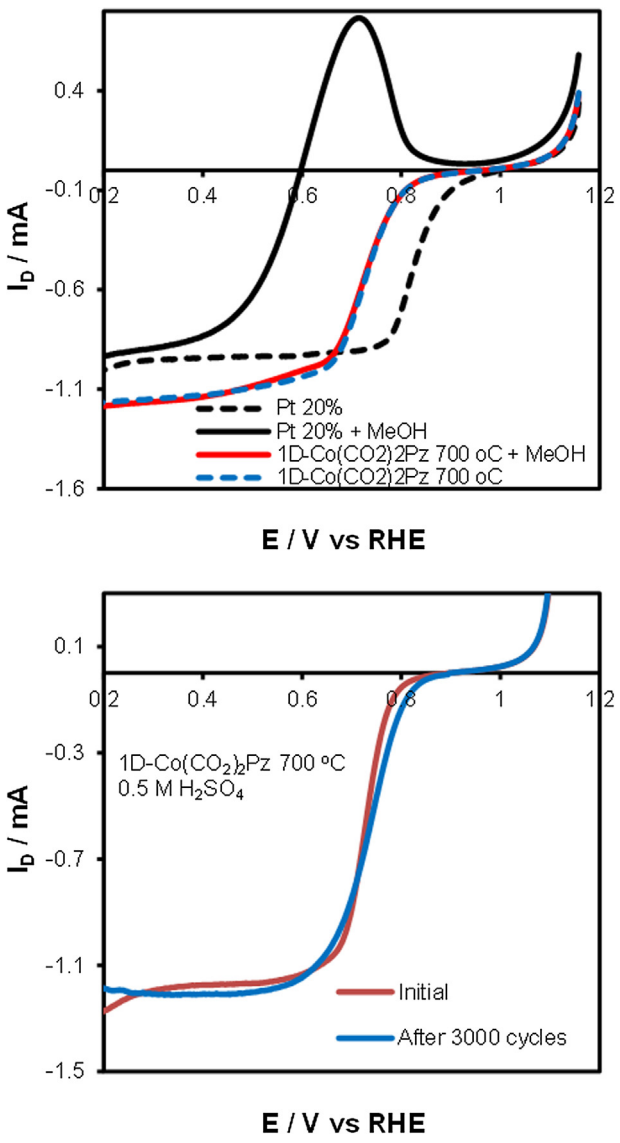

Fig. 8. Top: Methanol-tolerance measurement from the ORR polarization curves of Pt 20% and 1D-Co$(CO_2)_2$Pz 700 °C, measured at 25 °C in O_2 saturated 0.5 M H_2SO_4 solution on a gold disk. Methanol final concentration: 0.05 M. Rotation speed: 2500 rpm. Bottom: Accelerated durability test from the ORR polarization curve of the 1D-Co$(CO_2)_2$Pz 700 °C catalyst before and after 3000 cycles. (0.25–1.15 V vs RHE, sweep rate of 50 mV s^{-1}, O_2 saturated 0.5 M H_2SO_4, rotation speed of 2500 rpm).

From other point of view, both the ORR activity (i.e. $E_{1/2}$, limiting current in acidic medium), and the N content of the samples (700 °C) followed approximately the same trend as the weight retention (TGA, see Figure SI 2).

The ORR activity trend also followed the initial N content in the precursor compound, i.e. 3D-ZIF-67 > 0D-$CoCO_2$Pz > 1D-Co$(CO_2)_2$Pz > 3D-CoNic = 3D-Co$(CO_2)_2$bipy. The 0D-$CoCO_2$Pz complex did not follow this last trend, probably due to the lack of stability conferred by a polymeric structure.

Table 1 also shows data on related compounds previously published. High activities were reported using Fe ions as metal source, evidencing that Fe-N_x sites have higher activity for ORR than Co-N_x [12,18,49,50]. However the iron imidazolate MOF pyrolized at 900 °C exhibited a $E_{1/2}$ = 0.68 V [51]. Catalysts have been further improved using Zn^{2+} MOFs, particularly ZIF-8, loaded with Fe salts, complexes or even mixed with Fe or Co MOFs. During pyrolysis, usually performed at 900 °C or higher, Zn^0 is volatilized leaving empty pores and generating carbons with remarkably high specific area (up to 1563 $m^2 g^{-1}$, see Table 1), mesopores, and Fe centers very uniformly dispersed, avoiding the formation of metallic particles [52,53]. In this line, recently, pyrolysis at 950 °C of ZIF67@ZIF8 core-shell nanocrystals generated high ORR activity carbons with a hierarchically micro/mesoporous structure, leading to sufficient exposure and accessibility of the active sites and efficient transport pathways [54,55].

4. Conclusions and Perspectives

Three metal organic frameworks (MOFs), one linear coordination polymer and one complex were synthesized using N-heterocyclic ligands, characterized by different physical and electrochemical techniques. These studies of the samples afforded the following conclusions:

(1) Pyrolysis at 900 °C produced samples with lower Co and N content, and significantly higher H_2O_2 formation during ORR. This evidences the role of CoN_x and Pyridinic N in the reduction of H_2O_2.
(2) ORR activity and N content followed the same trend as the weight retention after pyrolysis. Polymers, and particularly MOFs, are stable compounds that keep or generate a porous structure during pyrolysis and retain N atoms. This is also useful to generate CoN_x (or FeN_x) moieties uniformly distributed on the catalyst, and to avoid formation of metallic particles. For this reason, the 0D-$CoCO_2$Pz complex (not a polymer) exhibited the poorest ORR catalytic activity.
(3) Ligands with highest N content produced the catalyst with highest activity. This is in line with the concept that the active sites are located on N atoms, particularly Pyrdinic N, CoN_x (or FeN_x). However, the 0D-$CoCO_2$Pz complex escapes away from this trend.
(4) The specific area on mesopores plays a key role, since it provides accessibility to the active sites. In this way, catalysts derived from the 1D-Co$(CO_2)_2$ Pz polymer (and also the 3D-CoNic MOF) displayed high ORR activity, comparable to that of 3D-ZIF-67 derived carbons, although the former ones had significantly lower N content and BET surface area. Pyrolysis of the ZIF-8 MOF, loaded with Fe compounds has been a successful strategy to produce highly active catalysts. The employ of templates and other related techniques may be useful to generate mesoporous M-N-dopped carbons with high ORR activity.

These results confirm the large number of variables and parameters that influence the activity of a catalyst. They further support efforts to synthesize new materials, not only with small particle size and large surface area, but also with adequate pore distribution and large surface on mesopores.

These new materials might be useful in other devices for energy conversion or storage, like supercapacitors, electrolyzer or Li batteries, where fast transport to active sites is required, exploiting their large surface area on mesopores. In this way, preliminary galvanostatic charge/discharge experiments have shown a specific capacitance of 550 F g^{-1} (2 A g^{-1}) for the 1D-Co$(CO_2)_2$Pz (900 °C) catalyst (6 M KOH). Finally, the 0D-$CoCO_2$Pz derived materials obtained as monoliths can be useful to build sensors or electrodes.

Acknowledgements

This work was supported by the Agencia Nacional de Promoción Científica y Tecnológica (project PICT-2013-2033), the Comisión Nacional de Energía Atómica (CNEA), and the Consejo Nacional de Investigaciones Científicas y Técnicas (CONICET). FR is a researcher

of CONICET and A.K.D.D. holds a doctoral fellowship of this institution. The authors acknowledge Cecilia A. Albornoz for the TGA measurements, Daniel R. Vega and Alicia Petragalli for obtaining the XRD patterns, Emilia B. Halac for the Raman spectra and Horacio Corti for valuable discussions. Federico A. Viva is acknowledged for his help in the fuel cell tests. Finally, the authors wish to thank Silvia A. Dominguez, Matias Aldunate and Gonzalo Zbihley for the SEM and TEM images.

Appendix A. Supplementary data

Supplementary data associated with this article can be found, in the online version, at http://dx.doi.org/10.1016/j.electacta.2017.08.055.

References

[1] B. Sørensen, Renewable Energy: Physics, Engineering, Environmental Impacts, Economics and Planning, 4th Edition, Academic Press Elsevier, Amsterdam, 2010.
[2] D.P. Wilkinson, J. Zhang, R. Hui, J. Fergus, X. Li, Proton Exchange Membrane Fuel Cells Materials Properties and Performance, CRC Press Taylor & Francis Group, 2010.
[3] M. Shao, Lecture Notes in Energy 9: Electrocatalysis in Fuel Cells A Non- and Low- Platinum Approach, Springer-Verlag, London, 2013.
[4] J.H. Zagal, F. Bedioui, Electrochemistry of N4 Macrocyclic Metal Complexes, Second ed., Springer International Publishing Group, Switzerland, 2016.
[5] J.D. Wiggins-Camacho, K.J. Stevenson, Mechanistic Discussion of the Oxygen Reduction Reaction at Nitrogen-Doped Carbon Nanotubes, J. Phys. Chem. C 115 (2011) 20002–20010.
[6] J. Li, S. Ghoshal, W. Liang, M.-T. Sougrati, F. Jaouen, B. Halevi, S. McKinney, G. McCool, C. Ma, X. Yuan, Z.-F. Ma, S. Mukerjee, Q. Jia, Structural and Mechanistic Basis for the High Activity of Fe-N-C Catalysts Toward Oxygen Reduction, Energy Environ. Sci. 9 (2016) 2418–2432.
[7] K. Artyushkova, A. Serov, S. Rojas-Carbonell, P. Atanassov, Chemistry of Multitudinous Active Sites for Oxygen Reduction Reaction in Transition Metal–Nitrogen–Carbon Electrocatalysts, J. Phys. Chem. C 119 (2015) 25917–25928.
[8] U.I. Kramm, M. Lefèvre, N. Larouche, D. Schmeisser, J.-P. Dodelet, Correlations between Mass Activity and Physicochemical Properties of Fe/N/C Catalysts for the ORR in PEM Fuel Cell via 57Fe Mössbauer Spectroscopy and Other Techniques, J. Am. Chem. Soc. 136 (2014) 978–985.
[9] A. Zitolo, V. Goellner, V. Armel, M.-T. Sougrati, T. Mineva, L. Stievano, E. Fonda, F. Jaouen, Identification of the Catalytic Sites of Oxygen Reduction in Iron-Doped Graphene Materials, Nat. Mat. 14 (2015) 937–942.
[10] Q. Jia, N. Ramaswamy, U. Tylus, K. Strickland, J. Li, A. Serov, K. Artyushkova, P. Atanassov, J. Anibal, C. Gumeci, S.C. Barton, M.-T. Sougrati, F. Jaouen, B. Halevi, S. Mukerjee, Spectroscopic Insights into the Nature of Active Sites in Iron–Nitrogen–Carbon Electrocatalysts for Oxygen Reduction in Acid, Nano Energy 29 (2016) 65–82.
[11] K. Strickland, E. Miner, Q. Jia, U. Tylus, N. Ramaswamy, W. Liang, M.-T. Sougrati, F. Jaouen, S. Mukerjee, Highly Active Oxygen Reduction Non-Platinum Group Metal Electrocatalyst without Direct Metal–Nitrogen Coordination, Nat. Commun. 6 (2015) 7343.
[12] H. Zhang, H. Osgood, X. Xie, Y. Shao, G. Wu, Engineering Nanostructures of PGM-Free Oxygen-Reduction Catalysts Using Metal-Organic Frameworks, Nano Energy 31 (2017) 331–350.
[13] S.R. Batten, N.R. Champness, X.-M. Chen, J. Garcia-Martinez, S. Kitagawa, L. Öhrström, M. O'Keeffe, M.P. Suh, J. Reedijk, Terminology of metal-organic frameworks and coordination polymers (IUPACrecomendations 2013), Pure Applied Chemistry 85 (2013) 1715–1724.
[14] L.R. MacGillivray, Metal Organic Framework Materials, John Wiley & Sons Ltd, Chichester, UK, 2014.
[15] D. Farrusseng, Metal-Organic Frameworks Applications from Catalysis to Gas Storage, Wiley-VCH Verlag & Co, Weinheim, Germany, 2011.
[16] P. Falcaro, R. Ricco, C.M. Doherty, K. Liang, A.J. Hill, M.J. Styles, MOF Positioning Technology and Device Fabrication, Chem. Soc. Rev. 43 (2014) 5513–5560.
[17] S.-L. Li, Q. Xu, Metal-Organic Frameworks as Platforms for Clean Energy, Energy Environ. Sci. 6 (2013) 1656–1683.
[18] A. Mahmood, W. Guo, H. Tabassum, R. Zou, Metal-Organic Framework-Based Nanomaterials for Electrocatalysis, Adv. Energy Mater. 6 (2016) 1600423-n/a.
[19] M.J. Song, I.T. Kim, Y.B. Kim, J. Kim, M.W. Shin, Metal–organic frameworks-derived porous carbon/Co3O4 composites for rechargeable lithium–oxygen batteries, Electrochim. Acta 230 (2017) 73–80.
[20] J. Wei, Y. Hu, Y. Liang, B. Kong, Z. Zheng, J. Zhang, S.P. Jiang, Y. Zhao, H. Wang, Graphene oxide/core-shell structured metal-organic framework nano-sandwiches and their derived cobalt/N-doped carbon nanosheets for oxygen reduction reactions, J. Mater. Chem. A 5 (2017) 10182–10189.
[21] W. Xia, J. Zhu, W. Guo, L. An, D. Xia, R. Zou, Well-Defined Carbon Polyhedrons Prepared From Nano Metal-Organic Frameworks for Oxygen Reduction, J. Mater. Chem. A 2 (2014) 11606–11613.
[22] X. Wang, J. Zhou, H. Fu, W. Li, X. Fan, G. Xin, J. Zheng, X. Li, MOF Derived Catalysts for Electrochemical Oxygen Reduction, J. Mater. Chem. A 2 (2014) 14064–14070.
[23] R. Banerjee, A. Phan, B. Wang, C. Knobler, H. Furukawa, M. Keeffe, O.M. Yaghi, High-Throughput Synthesis of Zeolitic Imidazolate Frameworks and Application to CO2 Capture, Science 319 (2008) 939–943.
[24] Y.-H. Liu, H.-L. Tsai, Y.-L. Lu, Y.-S. Wen, J.-C. Wang, K.-L. Lu, Assembly of a Robust, Thermally Stable Porous Cobalt(II) Nicotinate Framework Based on a Dicobalt Carboxylate Unit, Inorg. Chem. 40 (2001) 6426–6431.
[25] C.J. O'Connor, E. Sinn, Crystal Structures and Magnetic Properties of Cobalt(II) Pyrazinecarboxylate and Pyrazinedicarboxylate Complexes, Inorg. Chem. 20 (1981) 545–551.
[26] L. Mao, S.J. Rettig, R.C. Thompson, J. Trotter, S. Xia, 2, 3-Pyrazinedicarboxylates of Cobalt(II), Nickel(II), and Copper(II); Magnetic Properties and Crystal Structures, Can, J. Chem. 74 (1996) 433–444.
[27] T. Schareina, C. Schick, B.F. Abrahams, R. Kempe, Coordination Polymers of Bipyridyldicarboxylates –a Cobalt Containing 12,3-net with Potential Reactive Sites, Z, Anorg. Allg. Chem. 627 (2001) 1711–1713.
[28] E.A. Franceschini, M.M. Bruno, F.A. Viva, F.J. Williams, M. Jobbágy, H.R. Corti, Mesoporous Pt electrocatalyst for Methanol Tolerant Cathodes of DMFC, Electrochim. Acta 71 (2012) 173–180.
[29] K. Shen, X. Chen, J. Chen, Y. Li, Development of MOF-Derived Carbon-Based Nanomaterials for Efficient Catalysis, ACS Catalysis 6 (2016) 5887–5903.
[30] J. Tang, R.R. Salunkhe, H. Zhang, V. Malgras, T. Ahamad, S.M. Alshehri, N. Kobayashi, S. Tominaka, Y. Ide, J.H. Kim, Y. Yamauchi, Bimetallic Metal-Organic Frameworks for Controlled Catalytic Graphitization of Nanoporous Carbons, Sci. Rep 6 (2016) 30295.
[31] M.A. Pimenta, G. Dresselhaus, M.S. Dresselhaus, L.G. Cancado, A. Jorio, R. Saito, Studying Disorder in Graphite-Based Systems by Raman Spectroscopy, Phys. Chem. Chem. Phys. 9 (2007) 1276–1290.
[32] B.Y. Xia, Y. Yan, N. Li, H.B. Wu, X.W. Lou, X. Wang, A Metal–Organic Framework-Derived Bifunctional Oxygen Electrocatalyst, Nat. Energy 1 (2016) 15006.
[33] H.C. Choi, Y.M. Jung, I. Noda, S.B. Kim, A Study of the Mechanism of the Electrochemical Reaction of Lithium with CoO by Two-Dimensional Soft X-ray Absorption Spectroscopy (2D XAS), 2D Raman, and 2D Heterospectral XAS-Raman Correlation Analysis, J. Phys. Chem. B 107 (2003) 5806–5811.
[34] F. Roncaroli, E.S. Dal Molin, F.A. Viva, M.M. Bruno, E.B. Halac, Cobalt and Iron Complexes with N-heterocyclic Ligands as Pyrolysis Precursors for Oxygen Reduction Catalysts, Electrochim. Acta 174 (2015) 66–77.
[35] N. Mahmood, C. Zhang, H. Yin, Y. Hou, Graphene-Based Nanocomposites for Energy Storage and Conversion in Lithium Batteries Supercapacitors and Fuel Cells, J. Mater. Chem. A 2 (2014) 15–32.
[36] K. Niu, B. Yang, J. Cui, J. Jin, X. Fu, Q. Zhao, J. Zhang, Graphene-Based Non-Noble-Metal Co/N/C Catalyst for Oxygen Reduction Reaction in Alkaline Solution, J. Power Sources 243 (2013) 65–71.
[37] T. Zhang, C. He, F. Sun, Y. Ding, M. Wang, L. Peng, J. Wang, Y. Lin, Co3O4 nanoparticles anchored on nitrogen-doped reduced graphene oxide as a multifunctional catalyst for H2O2 reduction, oxygen reduction and evolution reaction, Sci. Rep 7 (2017) 43638.
[38] H. Wang, F.-X. Yin, B.-H. Chen, X.-B. He, P.-L. Lv, C.-Y. Ye, D.-J. Liu, ZIF-67 Incorporated with Carbon Derived from Pomelo Peels: A Highly Efficient Bifunctional Catalyst for Oxygen Reduction/Evolution Reactions, Appl. Catal. B 205 (2017) 55–67.
[39] R. Shi, G. Chen, W. Ma, D. Zhang, G. Qiu, X. Liu, Shape-Controlled Synthesis and Characterization of Cobalt Oxides Hollow Spheres and Octahedra, Dalton Trans. 41 (2012) 5981–5987.
[40] D. Barreca, A. Gasparotto, O.I. Lebedev, C. Maccato, A. Pozza, E. Tondello, S. Turner, G. Van Tendeloo, Controlled Vapor-Phase Synthesis of Cobalt Oxide Nanomaterials with Tuned Composition and Spatial Organization, CrystEngComm 12 (2010) 2185–2197.
[41] M.C. Onbaşlı, T. Goto, A. Tang, A. Pan, E. Battal, A.K. Okyay, G.F. Dionne, C.A. Ross, Oxygen Partial Pressure Dependence of Magnetic, Optical and Magneto-Optical Properties of Epitaxial Cobalt-Substituted SrTiO3 Films, Opt. Express 23 (2015) 13399–13409.
[42] K.S.W. Sing, D.H. Everett, R.A.W. Haul, L. Moscou, R.A. Pierotti, J. Rouquroi, T. Siemineieweka, Pure Applied Chemistry 57 (1988) 603–619.
[43] F. Jaouen, J.-P. Dodelet, O2 Reduction Mechanism on Non-Noble Metal Catalysts for PEM Fuel Cells. Part I: Experimental Rates of O2 Electroreduction, H2O2 Electroreduction, and H2O2 Disproportionation, J. Phys. Chem. C 113 (2009) 15422–15432.
[44] F. Jaouen, M. Lefèvre, J.-P. Dodelet, M. Cai, Heat-Treated Fe/N/C Catalysts for O2 Electroreduction: Are Active Sites Hosted in Micropores? J. Phys. Chem. B 110 (2006) 5553–5558.
[45] M. Lefèvre, E. Proietti, F. Jaouen, J.-P. Dodelet, Iron-Based Catalysts with Improved Oxygen Reduction Activity in Polymer Electrolyte Fuel Cells, Science 324 (2009) 71.
[46] G.A. Ferrero, K. Preuss, A.B. Fuertes, M. Sevilla, M.M. Titirici, The Influence of Pore Size Distribution on the Oxygen Reduction Reaction Performance in Nitrogen Doped Carbon Microspheres, J. Mater. Chem. A 4 (2016) 2581–2589.
[47] H.-W. Liang, W. Wei, Z.-S. Wu, X. Feng, K. Müllen, Mesoporous Metal–Nitrogen-Doped Carbon Electrocatalysts for Highly Efficient Oxygen Reduction Reaction, J. Am. Chem. Soc. 135 (2013) 16002–16005.
[48] A. Morozan, M.T. Sougrati, V. Goellner, D. Jones, L. Stievano, F. Jaouen, Effect of Furfuryl Alcohol on Metal Organic Framework-based Fe/N/C Electrocatalysts for Polymer Electrolyte Membrane Fuel Cells, Electrochim. Acta 119 (2014) 192–205.

[49] H.M. Barkholtz, D.-J. Liu, Advancements in Rationally Designed PGM-Free Fuel Cell Catalysts Derived from Metal-Organic Frameworks, Mater Horiz. 4 (2017) 20–37.
[50] C. He, T. Zhang, F. Sun, C. Li, Y. Lin, Fe/N co-doped mesoporous carbon nanomaterial as an efficient electrocatalyst for oxygen reduction reaction, Electrochim. Acta 231 (2017) 549–556.
[51] D. Zhao, J.-L. Shui, C. Chen, X. Chen, B.M. Reprogle, D. Wang, D.-J. Liu, Iron Imidazolate Framework as Precursor for Electrocatalysts in Polymer Electrolyte Membrane Fuel Cells, Chem. Sci. 3 (2012) 3200–3205.
[52] P. Yin, T. Yao, Y. Wu, L. Zheng, Y. Lin, W. Liu, H. Ju, J. Zhu, X. Hong, Z. Deng, G. Zhou, S. Wei, Y. Li, Single Cobalt Atoms with Precise N-Coordination as Superior Oxygen Reduction Reaction Catalysts, Angew. Chem. Int. Ed. 55 (2016) 10800–10805.
[53] L. Chong, G.A. Goenaga, K. Williams, H.M. Barkholtz, L.R. Grabstanowicz, J.A. Brooksbank, A.B. Papandrew, R. Elzein, R. Schlaf, T.A. Zawodzinski, J. Zou, S. Ma, D.-J. Liu, Investigation of Oxygen Reduction Activity of Catalysts Derived from Co and Co/Zn Methyl-Imidazolate Frameworks in Proton Exchange Membrane Fuel Cells, ChemElectroChem 3 (2016) 1541–1545.
[54] Z. Hu, Z. Zhang, Z. Li, M. Dou, F. Wang, One-Step Conversion from Core–Shell Metal–Organic Framework Materials to Cobalt and Nitrogen Codoped Carbon Nanopolyhedra with Hierarchically Porous Structure for Highly Efficient Oxygen Reduction, ACS Appl. Mater. Interfaces 9 (2017) 16109–16116.
[55] Y. Deng, Y. Dong, G. Wang, X. Sun, L. Zheng, X. Li, S. Liao, Well-Defined ZIF-Derived Fe–N Codoped Carbon Nanoframes as Efficient Oxygen Reduction Catalysts, ACS Appl. Mater. Interfaces 9 (2017) 9699–9709.
[56] X. Wang, H. Zhang, H. Lin, S. Gupta, C. Wang, Z. Tao, H. Fu, T. Wang, J. Zheng, G. Wu, X. Li, Directly Converting Fe-Doped Metal–Organic Frameworks into Highly Active and Stable Fe-N-C Catalysts for Oxygen Reduction in Acid, Nano Energy 25 (2016) 110–119.